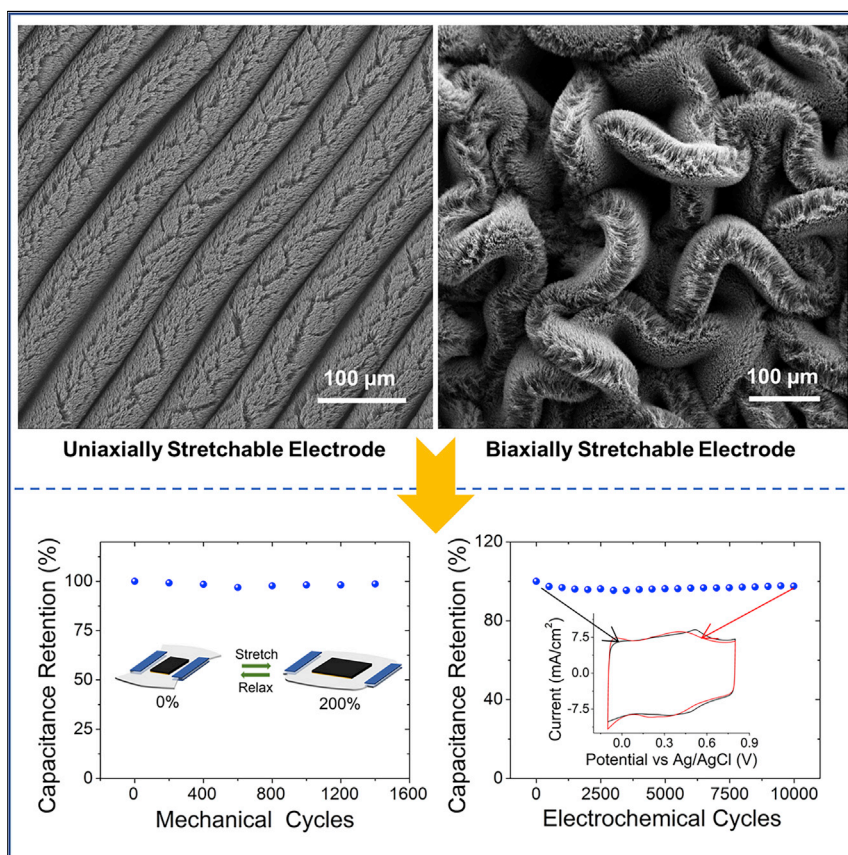


Article

Robust and High-Performance Electrodes via Crumpled Au-CNT Forests for Stretchable Supercapacitors



A robust and high-performance stretchable electrode was developed via crumpled Au-coated carbon nanotube (Au-CNT) forest transferred onto a compliant substrate. Compared with a pure CNT forest electrode, the Au-CNT forest electrode exhibits one order magnitude lower resistance. The stretchable Au-CNT forest electrodes and supercapacitors demonstrate significant improvement in mechanical reliability and electrochemical stability under extremely large strains. This research offers a facile approach to fabricate stretchable supercapacitors based on vertically aligned nanotubes or nanowires for exceptional and robust electrochemical performance.



Improvement

Enhanced performance with innovative design or material control

Yihao Zhou, Changyong Cao,
Yunteng Cao, Qiwei Han,
Charles B. Parker, Jeffrey T.
Glass

ccao@msu.edu (C.C.)
jeff.glass@duke.edu (J.T.G.)

HIGHLIGHTS

Fabricating high-performance stretchable electrodes via crumpled Au-CNT forest

Inventing a simple method to reduce electronic resistance of CNT forest electrodes

Studying the reasons for reduced resistance and improved performance of Au-CNT forest electrodes

Developing supercapacitors with high power density and fast charge/discharge capability

Article

Robust and High-Performance Electrodes via Crumpled Au-CNT Forests for Stretchable Supercapacitors

Yihao Zhou,¹ Changyong Cao,^{2,3,7,*} Yunteng Cao,⁴ Qiwei Han,^{1,6} Charles B. Parker,⁵ and Jeffrey T. Glass^{1,5,*}

SUMMARY

Stretchable supercapacitors based on vertically aligned nanotubes or nanowires have attracted considerable attention because of their improved robustness and electrochemical performance under large and repeated deformations. Here, we demonstrate a robust and high-performance stretchable electrode based on crumpled Au-coated carbon nanotube forest (Au-CNT forest). Experimental measurements show that the resistance of the Au-CNT forest electrode is around one order magnitude lower than that of a pure CNT forest electrode. The biaxially crumpled Au-CNT forest electrode demonstrates nearly identical electrochemical performance at different measured charge/discharge rates under different strain conditions (i.e., from 0% to 800% area strain). The as-prepared symmetric supercapacitor demonstrates a maximum specific capacitance of $\sim 6 \text{ mF cm}^{-2}$ at the current density of 40 mA cm^{-2} under large strains, exhibiting superior mechanical and electrochemical stability. This research presents a facile process to fabricate highly stretchable supercapacitors based on vertically aligned nanotubes or nanowires for achieving exceptional and robust electrochemical performance.

INTRODUCTION

Stretchable supercapacitors have received tremendous research interest in recent years because of their ability to serve as independent and conformal power sources for stretchable electronics, biointegrated electronics, and wearable electronics.^{1–8} Nanomaterials including metal,^{9,10} carbon,^{11,12} pseudocapacitive polymer,^{13,14} MXene,¹⁵ and metal oxide^{16,17} have been utilized to fabricate these kinds of devices. In particular, stretchable supercapacitors made from carbon nanomaterials (e.g., activated carbon, graphene, carbon nanotube [CNT]) are very promising and have been widely explored due to their low cost, high surface area, and long cycle lifetime.^{5,18,19} For example, CNT thin film electrodes demonstrated a consistent capacitance of 100 F g^{-1} under uniaxial strain up to 30%.²⁰ The crumpled graphene supercapacitor electrodes exhibited a capacitance of up to 200 F g^{-1} with area stretchability of 800%.²¹ Currently most stretchable electrodes are made from thin film materials, which suffer from cracking issues in the fabrication process because of the mismatched mechanical properties between the rigid active materials and the soft substrates.^{5,22} Delamination failure and cracks have also been frequently observed when the electrodes undergo large and repeated strains, resulting in significant degradation of their electrochemical performance.¹³

Recently, vertically aligned CNT forest electrodes have been explored to fabricate robust and extremely stretchable supercapacitors.²³ The main advantages of the

Progress and Potential

Emerging electronics such as wearable electronics and biointegrated electronics have evolved rapidly over the years. This bloom has generated great demands on high-performance stretchable energy devices such as batteries and supercapacitors. Although many nanomaterials and strategies are proposed to fabricate durable devices that can survive under large strains, they are suffering from the issues of robustness and low performance under large strains. Here, we successfully fabricated a robust and high-performance stretchable electrode and supercapacitor via the crumpled Au-CNT forest. Compared with the pure CNT forest, the Au-modified CNT forest electrode enabled a much smaller resistance. The all-solid-state supercapacitors demonstrated high power density and fast charge/discharge capability and represented a significant advancement toward the invention of highly stretchable, high-performance supercapacitors via vertically aligned CNT forests or other nanowires for numerous applications.

crumpled CNT forest include its easily accessible pore structure, short ion transport time, and low ionic diffusion resistance, leading to its high power and rate capability.^{24–26} The discretized feature of the CNT forest electrode makes it free of cracking even when subjected to large strains (e.g., 300%), thereby achieving better mechanical robustness, while the well-connected CNT network (the intertwined plasma-enhanced chemical vapor deposition [PECVD] grown CNTs and the randomly branching out CNTs) maintains conductivity and electrochemical performance.²⁷ Additionally, the crumpled CNT forest electrode can be easily modified via direct spray coating to be a hybrid high-performance supercapacitor with both pseudocapacitance and double-layer capacitance. For example, pseudocapacitive NiO nanoparticles can be airbrushed onto a CNT forest electrode and impregnated into the conductive CNT scaffold to enhance its electrochemical performance.²³ Despite these advantages, the crumpled CNT forest electrode shows relatively large electrical resistance, especially under extremely large mechanical strains (e.g., 800% area strain), which results in poor performance in high-speed charge/discharge measurements. This phenomenon is mainly due to the destruction of the well-connected CNT network and the poor physical contact between individual nanotubes under extremely large mechanical strains. This resistance issue significantly limits the power density and rate capability of the crumpled CNT forest electrode, becoming an obstacle for their use in some applications, especially those requiring high-speed charge/discharge. In fact, the reported stretchable CNT interwoven supercapacitor (CNT partially embedded in polydimethylsiloxane substrate) encountered a similar problem leading to poor device performance.²⁸

In this research, we demonstrate a facile approach to improve the electrical resistance of the crumpled CNT forest under large strain deformations. We deposit a thin layer of metal film on top of the CNT forest before the dry-transfer step to form an Au-modified CNT forest electrode. The Au-modified CNT forest (referred to as Au-CNT forest) increases the contact area between the CNT forest and the prestrained substrate, which facilitates the transfer of the forest. More importantly, the Au-modified CNT forest network reduces the resistance of the forest electrode by an order of magnitude while maintaining the unique porous structure of the crumpled CNT forest. As a result, nearly constant electrochemical performance under extremely large mechanical strains (i.e., 800% area strain) is achieved in high-speed charge/discharge measurements. The successful development of the Au-CNT forest electrodes and corresponding all-solid-state supercapacitors with high power density and fast charge/discharge capability represents a significant advancement toward the invention of highly stretchable, high-performance supercapacitors based on vertically aligned CNT forests for wearable electronics and beyond.

RESULTS

Fabrication and Characterization of Crumpled Au-CNT Forest Electrodes

Figure 1A depicts the fabrication process for a biaxially stretchable Au-CNT forest electrode. In brief, a seeding nanofilm of iron (Fe, ~5 nm) is first deposited onto an n-doped Si wafer. The CNT forest is then grown via the PECVD method.²⁹ Next, a layer of gold (~50 nm) is deposited onto the top of the CNT forest by a vacuum sputtering coater (Figure 1B). The diameter of the Au-coated CNTs is 148 ± 8.41 nm, which is approximately three times that of the original CNTs (Figure S1). The Au-CNT forest is then dry-transferred onto a prestretched elastomer substrate (VHB 4910; 3M, USA), following the same procedure reported in our previous work.²³ To facilitate the transfer of the CNT forest, the as-grown CNT forest on Si wafer is annealed in air on a hotplate at 540°C for 15 min to partially oxidize the

¹Department of Mechanical Engineering & Materials Science, Duke University, Durham, NC 27708, USA

²Laboratory for Soft Machines & Electronics, School of Packaging, Michigan State University, East Lansing, MI 48824, USA

³Departments of Mechanical Engineering, Electrical & Computer Engineering, Michigan State University, East Lansing, MI 48824, USA

⁴Department of Civil and Environmental Engineering, Massachusetts Institute of Technology, Cambridge, MA 02139, USA

⁵Department of Electrical & Computer Engineering, Duke University, Durham, NC 27708, USA

⁶Department of Chemistry, Duke University, Durham, NC 27708, USA

⁷Lead Contact

*Correspondence: ccao@msu.edu (C.C.), jeff.glass@duke.edu (J.T.G.)

<https://doi.org/10.1016/j.matt.2020.02.024>

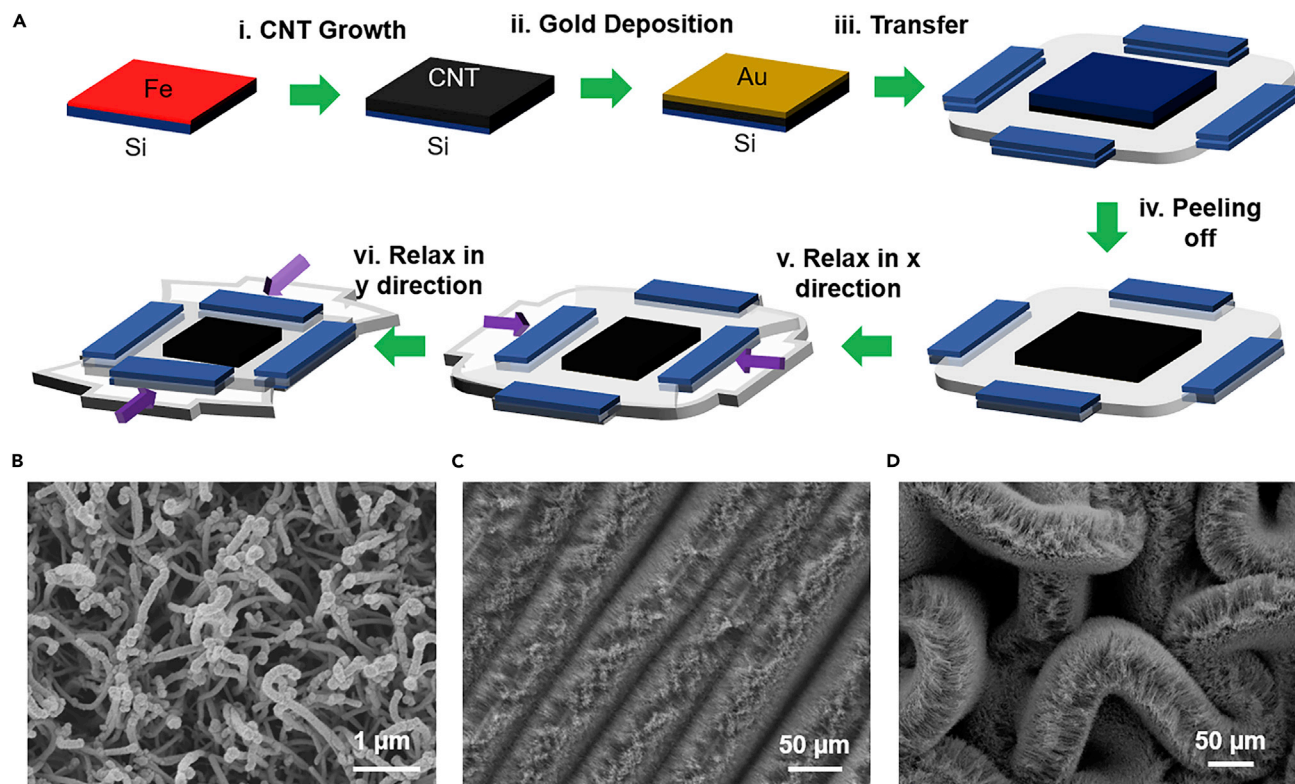


Figure 1. Fabrication and Characterization of Robust Stretchable Au-CNT Forest Electrodes

(A) Schematic illustration of the fabrication process of a biaxially stretchable electrode via Au-CNT forest. (i) PECVD growth of vertically aligned CNT forest on a silicon wafer. (ii) Sputter-coating a thin layer of gold film on top of the CNT forest. (iii) Dry-transferring Au-CNT forest to a prestrained elastomer substrate. (iv) Peeling off the silicon wafer from the substrate. (v) Releasing the prestrain of the substrate in one direction. (vi) Releasing the prestrain in its orthogonal direction.

(B) SEM image of the top view of the Au-coated CNT forest.

(C) SEM image of the Au-CNT forest pattern morphology generated by a uniaxial prestrain of 300%.

(D) SEM image of the Au-CNT forest pattern morphology formed by applying a biaxial prestrain of 200% × 200%.

region of the CNT forest connecting to iron seeds.³⁰ It is worth noting that the Au-CNT forest is upside down after the dry-transfer step. The intertwined top section of the original Au-CNT forest serves as a conductive network at the base of the crumpled Au-CNT forest electrode. [Figure S1](#) shows the scanning electron microscopy (SEM) images of CNT/Si and Au-CNT/Si substrates after the transfer process, indicating that most of the CNT forest is successfully transferred from the Si wafer onto the elastomer substrate.

Thereafter, the prestrain in the stretched substrate is relaxed along two orthogonal directions sequentially to form a crumpled Au-CNT forest electrode with hierarchical wrinkle or ridge structures ([Figures 1C and 1D](#)). As shown in [Figure 1C](#), the uniaxially stretchable Au-CNT forest electrode is fabricated by applying a 300% uniaxial prestrain while the biaxially stretchable Au-CNT forest electrode is fabricated by applying a 200% × 200% prestrain onto the elastomer substrate along its two orthogonal directions ([Figure 1D](#)). Different from the crumpled graphene paper with high-aspect-ratio ridges,^{21,31} the pattern of crumpled Au-CNT forest is mainly composed of wrinkles under large prestrains ([Figures 1C and 1D](#)), which is attributed to the small volume ratio of CNT forest (~1%).^{32,33} At the beginning of the relaxation, the discrete CNTs can be compressed easily due to a small compression modulus,³⁴ leading to delayed and more uniform wrinkle formation. Moreover,

the discrete but entangled feature of the Au-CNT forest enables it to avoid cracking or breaking, which enhances the reliability of the electrode under cyclic mechanical loading or overstretching of the stretchable thin films.³⁵

Figures S2A and S2B show the wrinkle patterns of a uniaxially stretchable CNT forest electrode and a uniaxially stretchable Au-CNT forest electrode, respectively. The wrinkle wavelength of the crumpled Au-CNT forest electrode is $\sim 20\%$ larger than that of the crumpled CNT forest electrode without a Au coating. This is because the Au deposition increases the effective thickness of the CNT forest layer and the effective compression modulus of the CNT forest. The electrical resistance of the stretchable Au-CNT forest electrode is significantly lower than that of the CNT forest electrode in the measured stretching range (i.e., $272\ \Omega$ versus $24\ \Omega$ at 0% strain, and $543\ \Omega$ versus $52\ \Omega$ at 300% strain) (Figure S2C). Similar variations of the morphology and the resistance are also observed for a biaxially stretchable electrode with a crumpled Au-CNT forest (Figures S2D–S2F). The conductivity improvement of the Au-CNT forest electrodes is mainly attributed to two aspects: (1) the Au coating significantly reduces the contact resistance between individual CNTs in the relaxation process; (2) the Au coating connects more independent CNTs into the CNT network (Figure 1A), which then enhances the conductivity by having more conductive pathways in the CNT network.^{36,37}

Performance of Uniaxially Stretchable Au-CNT Forest Electrodes

Figure 2 shows the electrochemical performance of uniaxially stretchable Au-CNT forest electrodes. As shown in Figure 2A, cyclic voltammetry (CV) curves of a uniaxially stretchable Au-CNT forest electrode under 300% strain are rectangular across all scan rates ranging from $20\ \text{mV s}^{-1}$ to $5\ \text{V s}^{-1}$ in $1\ \text{M H}_2\text{SO}_4$, indicating its excellent capacitive behavior and superior rate capability. Redox peaks are observed at around 0.5 and 0.3 V versus the Ag/AgCl reference electrode on the CV in $1\ \text{M H}_2\text{SO}_4$. These redox peaks are from the faradic redox reactions (protonations) of the surface groups on the CNT walls in the acidic electrolyte,³⁸ because there are no similar peaks observed in testing a stretchable CNT forest electrode in $1\ \text{M KCl}$ electrolyte.²³ Unlike the Au-CNT forest electrode, the CNT forest electrode under 300% strain showed distorted CV curves at a high scan rate ($5\ \text{V s}^{-1}$ in Figure S3), which may be attributed to the large CNT forest resistance under extreme mechanical deformations. Figure 2B shows the CV of Au-CNT forest electrode and CNT forest electrode at $5\ \text{V s}^{-1}$ under different strains, demonstrating different influences of the strain on the capacitive current of the two stretchable electrodes. The capacitive current of the uniaxially stretchable Au-CNT forest increases from $56\ \text{mA cm}^{-2}$ to $70\ \text{mA cm}^{-2}$ at 0.4 V versus the Ag/AgCl reference electrode when the strain changes from 0% to 300% and the CV remains rectangular at higher strain states. On the contrary, the capacitive current of the stretchable CNT forest electrode decreases with applied strain, reducing from $43\ \text{mA cm}^{-2}$ under 0% strain to $17\ \text{mA cm}^{-2}$ under 300% strain at the same applied potential. Enhancement of the electrochemical performance of the uniaxially stretchable Au-CNT forest electrode at higher strain states results from two factors: the reduced resistance of the electrodes by Au coating and smaller ion-diffusion resistance due to increased distance between neighboring nanotubes and the wavelength of wrinkles and, thus, larger pore size.^{24,39}

Figure 2C presents the specific capacitance calculated based on the CV curves at different scan rates for both uniaxially stretchable Au-CNT and CNT forest electrodes. It can be seen that the specific capacitance of CNT forest electrodes is nearly constant at different strain states for low scan rates (i.e., $20\ \text{mV s}^{-1}$). However, when the scan rate increases to $5\ \text{V s}^{-1}$, the capacitance drops dramatically with applied strain increase (i.e., from $6.67\ \text{mF cm}^{-2}$ at 0% down to $2.11\ \text{mF cm}^{-2}$ at 200%). The significant loss of

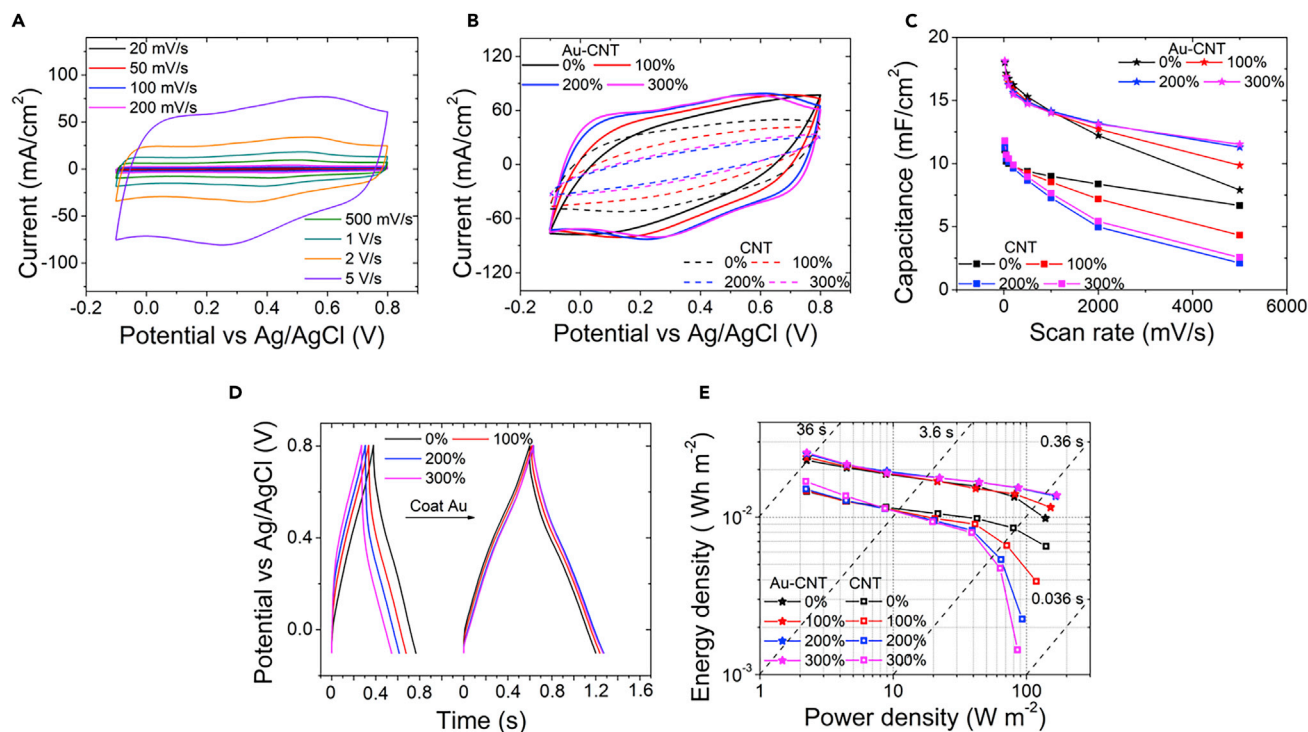


Figure 2. Electrochemical Performance of Uniaxially Stretchable Au-CNT Forest Electrodes

(A) CV curves of a representative uniaxially stretchable Au-CNT forest electrode at the 300% strain state, measured at different scan rates from 20 mV s^{-1} to 5 V s^{-1} .

(B) CV curves of the uniaxially stretchable Au-CNT forest electrode measured at a scan rate of 5 V s^{-1} at different strain states, compared with the uniaxially stretchable CNT forest electrode under the same conditions.

(C) Specific capacitance of the uniaxially stretchable Au-CNT forest electrode as a function of scan rates, measured at different strain states.

(D) GCD curves of the uniaxially stretchable Au-CNT and CNT forest electrodes measured at a current density of 20 mA cm^{-2} at different strain states.

(E) Ragone plot of uniaxially stretchable Au-CNT and CNT supercapacitor electrodes.

All of the measurements were performed in $1 \text{ M H}_2\text{SO}_4$.

capacitance under large strain at a high scan rate hinders its high power and high rate applications. In contrast, the Au-CNT forest electrode shows increased specific capacitance and higher rate capability when the applied strain increases from 0% to 300%. The Au-CNT forest electrode demonstrates an areal capacitance of 18.14 mF cm^{-2} at 20 mV s^{-1} under 300% applied strain, 50% higher than the value of a CNT forest electrode. When the scan rate increases to 5 V s^{-1} , the specific capacitance of the Au-forest electrode is 11.52 mF cm^{-2} almost four times higher than that of the CNT forest electrode. The capacitance retention of an Au-CNT forest electrode is $\sim 64\%$ from 20 mV s^{-1} to 5 V s^{-1} under 300% strain, whereas the capacitance retention of CNT forest electrode is only $\sim 22\%$. The increase of specific capacitance of the Au-CNT forest electrode may be attributed to three reasons. First, more CNTs are better connected via the coated Au layer in the Au-CNT network, leading to the increased amount of active material and available surface area for capacitance. Second, Au has a double-layer capacitance of $25 \text{ } \mu\text{F/cm}^2$,⁴⁰ twice the value of CNT.³² Third, increased distance between neighboring nanotubes and the wavelength of wrinkles and, thus, larger pore size decreases ion-diffusion resistance. It is noted that the CNTs grown by PECVD from different batches varies slightly (Figure S4), leading to small differences among the CNT forest samples in testing. Moreover, the Au-CNT forest demonstrates a distinct trend from the CNT forest electrode, whose specific capacitance decreases as the scan rate and applied strain increase. For instance, the specific capacitance increases from 7.9 mF cm^{-2} to 11.52 mF cm^{-2} at 5 V s^{-1} from 0% strain to 300% strain.

The difference between Au-CNT forest and CNT forest electrodes is also observed in the galvanostatic charge/discharge (GCD) measurements. Figure 2D shows the charge/discharge curves of Au-CNT and CNT forest electrodes subjected to different strains at a charge/discharge current density of 20 mA cm^{-2} . An increasing drop in internal resistance (IR) appears in the charge/discharge curves of the CNT forest electrode with increased strain, indicating an increasing IR. Therefore, the charge/discharge time of one cycle decreases from $\sim 0.8 \text{ s}$ at 0% strain to less than 0.6 s at 300% strain. For the Au-CNT forest electrode, the charge/discharge time slightly increases with the applied strain due to the reduced forest resistance and more vertically aligned porous structure under large strains. The specific capacitance of the stretchable supercapacitor electrodes can also be calculated from the GCD curves at different current densities. The challenge of using this method is to determine the IR drop at the beginning of the discharge process. As shown in Figure S5, a transition from IR drop to normal potential decrease is observed at the start of the discharge process in the charge/discharge curves, especially at a high current density.⁴¹ Such behavior is generally related to the resistance of the stretchable electrode because the extrapolated ohmic drop changes significantly with the applied strain. Previous results have demonstrated that the ohmic drop calculated by the extrapolation method can give a more accurate power performance.⁴² Figure S6 presents the specific capacitances of the uniaxially stretchable CNT/Au-CNT electrodes at different strain states, based on the GCD measurements with the ohmic drop.

Figure 2E shows the Ragone plot (energy density versus power density) of the uniaxially stretchable CNT and Au-CNT forest electrodes under different strains, which are calculated from the obtained ohmic drop and capacitance. Electrode resistance is believed to be a key factor in determining the power density of a supercapacitor. Therefore, the energy density of the CNT forest electrode begins to drop quickly at high strain states when the power density reaches 100 W m^{-2} due to its large resistance. On the other hand, the Au-CNT forest electrode shows almost constant energy density at different strain states, even when the power density is above 100 W m^{-2} , thanks to the higher capacitance and reduced resistance provided by the Au-CNT network.

Performance of Biaxially Stretchable Au-CNT Forest Electrodes

Figure 3A shows the CV curves of a biaxially stretchable electrode with crumpled Au-CNT forest measured at various scan rates from 20 mV s^{-1} to 5 V s^{-1} in $1 \text{ M H}_2\text{SO}_4$. Compared with the CV curves of the uniaxially stretchable Au-CNT forest electrode, the biaxially stretchable Au-CNT forest electrode demonstrates a slightly distorted rectangular shape, indicating a larger resistance of the electrode. Figure 3B displays the CV curves of the biaxially stretchable Au-CNT forests at the scan rate of 5 V s^{-1} at different strain states. The CV curves at different strain states have no significant difference, indicating the negligible influence of the strain on the performance of the stretchable Au-CNT forest electrode. This may be due to the tradeoff between the increased electronic resistance and the declined ion-diffusion resistance. On the contrary, the CV curves of the pure CNT forest electrode at the same scan rate are inclined remarkably, even with a small current density (Figure 3B).

The specific capacitances of the biaxially stretchable Au-CNT forest and CNT forest electrodes calculated from the CV curves at different strain states are summarized in Figure 3C. Compared with the CNT forest, the Au-CNT forest electrode demonstrates significantly improved performances in both specific capacitance and rate capability. The biaxially stretchable Au-CNT forest electrode shows a specific

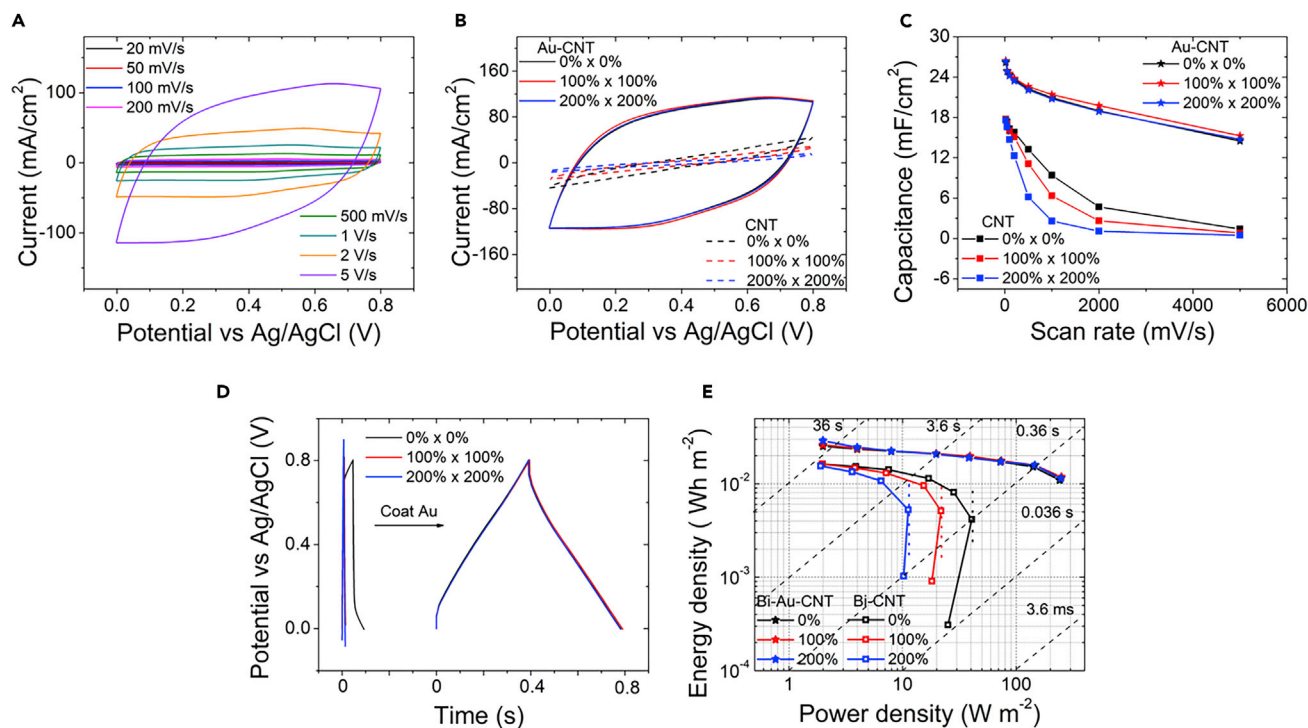


Figure 3. Electrochemical Performance of Biaxially Stretchable Au-CNT Forest Electrodes

(A) CV curves of a representative biaxially stretchable Au-CNT forest electrode at the 200% × 200% strain state, measured at different scan rates from 20 mV s⁻¹ to 5 V s⁻¹.

(B) CV curves of the biaxially stretchable Au-CNT forest electrode measured at a scan rate of 5 V s⁻¹ at different strain states, compared with the biaxially stretchable CNT forest electrode under the same conditions.

(C) Specific capacitance of the biaxially stretchable Au-CNT forest electrode as a function of scan rates, measured at different strain states. The data for the biaxially stretchable CNT forest electrodes are presented for comparison.

(D) GCD curves of the biaxially stretchable Au-CNT and CNT forest electrodes measured at a current density of 40 mA cm⁻² at different strain states.

(E) Ragone plot of biaxially stretchable Au-CNT and CNT supercapacitor electrodes.

All of the measurements were performed in 1 M H₂SO₄.

capacitance of ~26.33 mF cm⁻² at 20 mV s⁻¹ and ~14.72 mF cm⁻² at 5 V s⁻¹, much larger than those of its CNT forest counterparts at all of the tested scan rates (e.g., ~50% higher at 20 mV s⁻¹ and ~2,967% higher at 5 V s⁻¹). The capacitance retention of the biaxially stretchable Au-CNT forest electrode is ~56% (from 20 mV s⁻¹ to 5 V s⁻¹) under the strain of 200% × 200%, whereas only 2.7% capacitance can be retained from 20 mV s⁻¹ to 5 V s⁻¹ for the CNT forest electrode at the same strain state. The improved rate capability of the Au-CNT forest electrode is also attributed to the easily accessible porous structure (low ionic resistance) and increased conductivity across the crumpled Au-CNT forest (low electronic resistance).

Figure 3D illustrates the improvement of the GCD behavior of a biaxially stretchable Au-CNT forest electrode. The charge/discharge curves of the biaxially stretchable Au-CNT forest electrode are identical under different strains with small IR drops. On the other hand, the IR drop of the CNT forest electrode at the relaxed state is considerable, and at several strain states (e.g., 100% × 100% and 200% × 200%) exceeds the potential window of charge/discharge at 40 mA cm⁻², and no capacitance can be measured. The specific capacitance of the biaxially stretchable Au-CNT forest electrode under different strains from GCD measurements is almost constant even when the charge/discharge current density is 80 mA cm⁻², indicating a consistent electrochemical performance of the electrode under large strains (Figure S6).

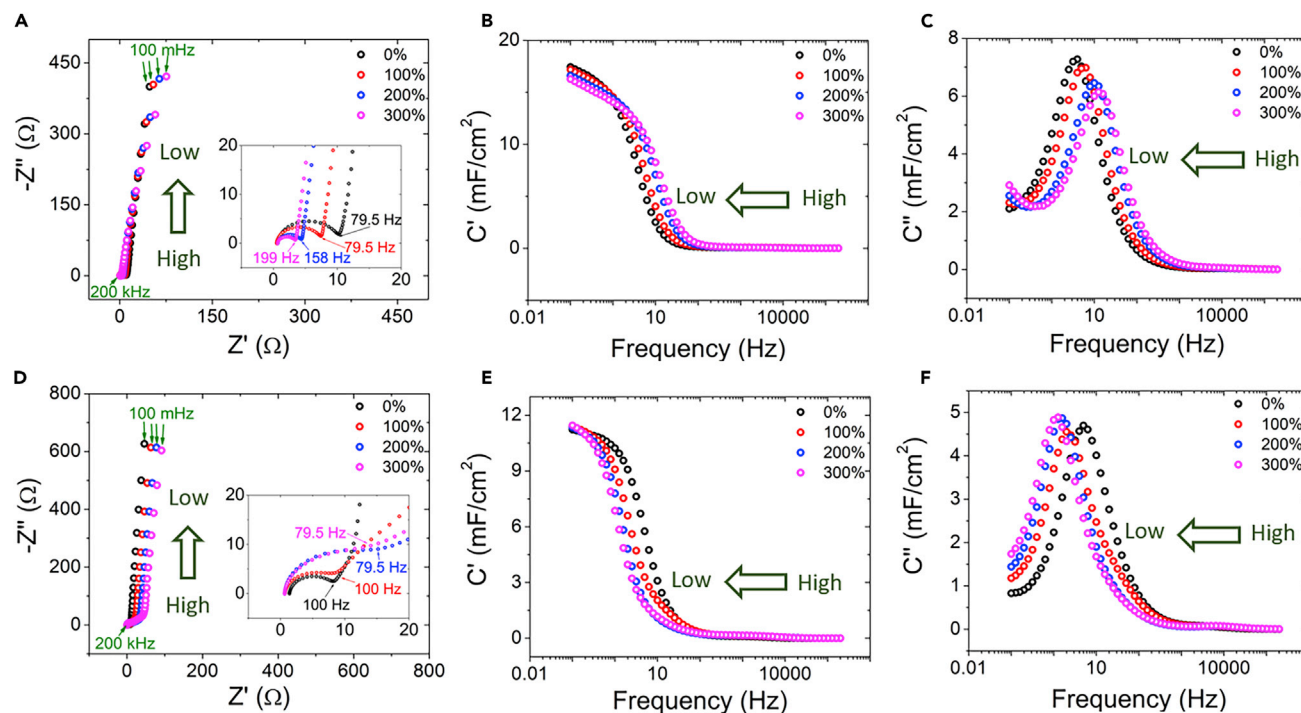


Figure 4. EIS Results of Uniaxially Stretchable CNT and Au-CNT Forest Electrodes

(A) Nyquist plot of a uniaxially stretchable Au-CNT forest electrode at different strain states.
 (B) Variation of real capacitance as a function of frequency for the uniaxially stretchable Au-CNT forest electrode at different strain states.
 (C) Variation of imaginary capacitance as a function of frequency for the uniaxially stretchable Au-CNT forest electrode at different strain states.
 (D) Nyquist plot of a uniaxially stretchable CNT forest electrode at different strain states.
 (E) Variation of real capacitance as a function of frequency for the uniaxially stretchable CNT forest electrode at different strain states.
 (F) Variation of imaginary capacitance as a function of frequency for the uniaxially stretchable CNT forest electrode at different strain states.
 EIS was performed from 200 kHz to 100 mHz as indicated by the arrow.

Figure 3E presents the Ragone plot of a biaxially stretchable CNT electrode and a biaxially stretchable Au-CNT electrode using IR drop and specific capacitance obtained from GCD measurements. Similar to the uniaxial case, the biaxially stretchable crumpled Au-CNT forest electrode possesses constant power performance at different strain states even when the power density is as high as $\sim 250 \text{ W m}^{-2}$ due to the reduced forest resistance. For the pure crumpled CNT forest electrode, the maximum power density is limited by the increased ohmic drop when discharge current increases. The maximum power density of the CNT forest electrode decreases from 40 W m^{-2} at $0\% \times 0\%$ strain to 11.2 W m^{-2} at $200\% \times 200\%$ strain, less than 5% of the values obtained from the Au-CNT electrode at the same strain level. When discharged in the same time interval (0.36 s), the biaxially stretchable Au-CNT forest exhibits about ten times higher energy and power density compared with the crumpled CNT forest electrode at the strain state of $200\% \times 200\%$.

EIS and Stability Analysis of Stretchable Au-CNT Forest Electrodes

To further analyze the electrochemical performance of the stretchable CNT and Au-CNT forest electrodes, we carried out electrochemical impedance spectroscopy (EIS) measurements of all samples at 0.4 V versus the Ag/AgCl reference electrode. The Nyquist plots of uniaxially stretchable Au-CNT and CNT electrodes are shown in Figures 4A and 4D. All of the measured curves have two common features. First, the intersection at the z' axis at a high frequency (i.e., 200 kHz) is $\sim 1 \Omega$, indicating good

electrolyte conductivity. Second, a near-ideal capacitive behavior is observed from the straight line in the low-frequency range. The major difference is located at the high-to-middle frequency range as indicated by the semicircle. For the CNT forest electrode, the radius of the semicircle increases with the increasing strain (Figure 4D) while the semicircle of the Au-CNT forest electrode becomes smaller with the increasing strains, as shown in the inset of Figure 4A. This variation of device resistance results from the change of the electronic resistance and ion resistance at different strain states.⁴³ The electronic resistance includes the forest film resistance and the contact resistance at the interface of the Ti current collector and the CNT forest electrode. When the electrode is stretched, the CNT forest resistance increases due to the reduction in the number of conductive pathways. The ionic resistance is determined by the ionic conductivity to the interface of the CNT forest electrode and electrolyte. The ionic conductivity is dependent mainly on the diffusion resistance and is affected by the porous structure of the electrode. When the CNT forest electrode is relaxed, the distance between individual CNTs is smaller, leading to smaller pores hindering ion diffusion into the structure. When the electrode is subjected to a large strain (e.g., 300%) the distance between CNTs increases, leading to an accessible porous structure. Furthermore, the unfolding of the wrinkles allows ions to diffuse into the CNT pores easier via the valleys of the wrinkled structure. Consequently, the ionic resistance decreases with the applied strain. For the stretchable CNT forest without the Au-CNT network, the electronic resistance dominates the response of the CNT forest in the high-frequency range; thus, the semicircle radius grows with increasing applied strains. When the Au-modified network is introduced, the electronic resistance can be significantly reduced (Figures S2C and S2F), resulting in the dominance of ionic resistance in that frequency range. Therefore, the radius of the semicircle decreases with the applied strain. A similar trend is also confirmed by the Nyquist plots of the biaxially stretchable CNT and Au-CNT forest electrodes, as shown in Figures S7A and S7D.

The real C' and imaginary C'' capacitance versus frequency can be calculated using the equation⁴⁴ $C' = \frac{-Z''(\omega)}{\omega|Z(\omega)|^2}$, $C'' = \frac{Z'(\omega)}{\omega|Z(\omega)|^2}$. For the uniaxially stretchable CNT and Au-CNT forest electrodes, the relations between C' and frequency are plotted in Figures 4B and 4E. In the low-frequency range, the Au-CNT forest electrode shows a capacitance of $\sim 18 \text{ mF cm}^{-2}$, whereas the CNT forest electrode exhibits a capacitance of $\sim 11 \text{ mF cm}^{-2}$. These results agree with the calculated values from the CV curves. As the frequency increases the real capacitance decreases, leading to a transition from capacitive response to resistive response at high frequencies. The transition behavior of the Au-CNT forest electrode shifts to a higher frequency with a larger applied strain, demonstrating a wider range of capacitive response. On the other hand, the transition behavior of the CNT forest electrode shifts to lower frequency with increasing applied strains. The different trends of the C' curves are attributed to the change of the ionic and the electronic resistance with applied strains, as discussed above. Interestingly, the C' curves of the biaxially stretchable Au-CNT forest electrode at different strain states remain identical (Figure S7B), indicating that the increase of electronic resistance and the decrease of ionic resistance reach a balance for that electrode. There is no plateau observed for the biaxially stretchable CNT forest electrode under large mechanical strains, indicating its poor capacitive behavior (Figure S7E).

Figure 4C shows the variation of the imaginary part (C'') of the capacitance of a uniaxially stretchable Au-CNT forest electrode as a function of frequency. The imaginary capacitance corresponds to some irreversible dissipation process (e.g., the dielectric loss in water due to the movement and rotation of the molecules) at the

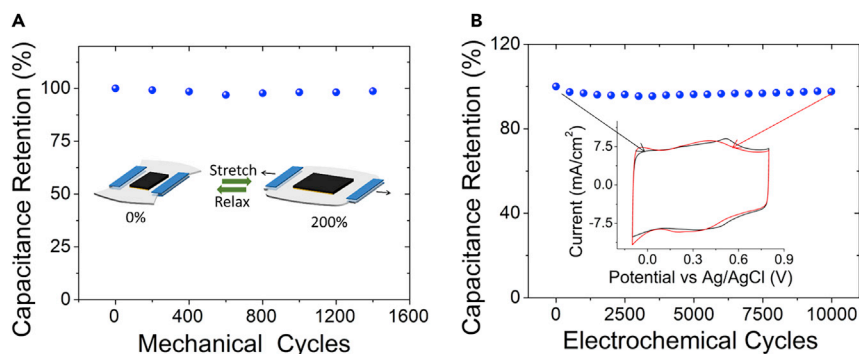


Figure 5. Mechanical and Electrochemical Stability Analysis of a Stretchable Au-CNT Forest Electrode

(A) Capacitance retention of a uniaxially stretchable Au-CNT forest electrode under mechanical stretching-relaxation cyclic deformations to a strain of 200%.

(B) Capacitance retention of a uniaxially stretchable Au-CNT forest electrode tested for 10,000 times of charge/discharge cycles at the relaxed state. Inset shows the CV curves measured before and after the electrochemical stability test at the scan rate of 500 mV s^{-1} .

electrode/electrolyte interface.⁴⁵ The maximum of the C'' curve denotes the transition from capacitive behavior to resistive behavior and is related to the relaxation time of the electrode by $\tau = \frac{1}{f}$, where f is the frequency of maximum C'' .⁴⁶ In [Figure 4C](#), the relaxation time of the electrode at different strain states is 251 ms, 158 ms, 100 ms, and 79 ms, declining with the increased strain from 0% to 300%, which is in agreement with the CV and GCD measurements. These relaxation time values are shorter than previously reported values for activated carbon and CNT composite,^{44,46,47} indicating the superior rate capability and high power density of this stretchable Au-CNT forest electrode. The relaxation time of the uniaxially stretchable CNT forest, calculated from [Figure 4F](#), increases from 158 ms to 794 ms when the applied strain increases from 0% to 300%. For the biaxially stretchable Au-CNT forest electrode, the relaxation time is 158 ms for all strain states ([Figure S7C](#)). The relaxation time of the biaxially stretchable CNT forest electrode is calculated to be 1.58 s, 2.51 s, and 5.01 s for the strains of 0% \times 0%, 100% \times 100%, and 200% \times 200%, respectively ([Figure S7F](#)). Under large mechanical strains, the relaxation time of the Au-CNT forest electrode is ~ 10 times (300% uniaxial strain) and 31 times (200% \times 200% biaxial strain) shorter than its CNT forest counterpart, due to the improved electronic and ionic conductivities.

[Figure 5](#) presents the mechanical and electrochemical stability of a stretchable Au-CNT forest electrode, which is a critical factor for potential applications of stretchable devices.⁴⁸ The stretchable Au-CNT forest electrode maintains its initial capacitance (2 mA cm^{-2} , calculated by GCD) well, retaining $\sim 100\%$ after 1,400 stretching-relaxation cycles of a uniaxial strain of 200% ([Figure 5A](#)), indicating excellent electrical integrity and constant resistance over large cyclic mechanical strains. [Figure 5B](#) shows the electrochemical stability of the Au-CNT forest electrode measured by charging/discharging the electrode at a scan rate of 5 mA cm^{-2} for 10,000 times, for which the normalized capacitance retention of the electrode is around 97.6%. The inset of [Figure 5B](#) illustrates the CV curves of the electrode measured before and after 10,000 charging/discharging cycles. These results demonstrate that the Au-CNT forest electrodes have excellent electrochemical stability and robust adhesion strength between the Au-CNT forest and the elastomer substrate.

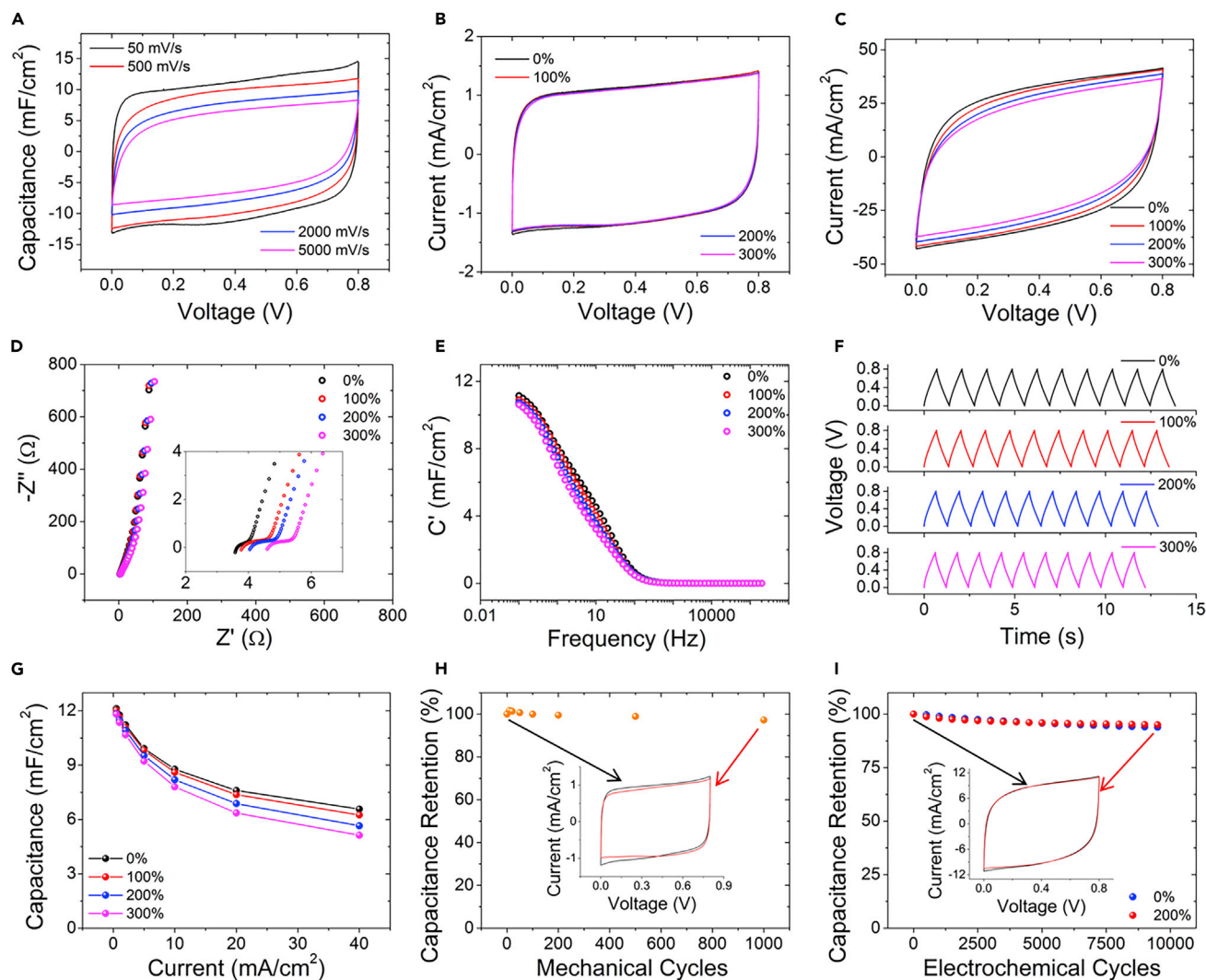


Figure 6. Electrochemical Performance of a Representative Uniaxially Stretchable Au-CNT Forest Supercapacitor

(A) CV curves of the supercapacitor measured at different scan rates from 50 mV s^{-1} to 5 V s^{-1} at the relaxed state.

(B) CV curves of the supercapacitor measured at the scan rate of 100 mV s^{-1} at different strain states from 0% to 300%.

(C) CV curves of the supercapacitor measured at the scan rate of 5 V s^{-1} at different strain states from 0% to 300%.

(D) EIS curves of the supercapacitor measured at different strain states varying from 0% to 300%.

(E) Capacitance variation of the supercapacitor with the frequency at different strain states from 0% to 300%, derived from the EIS curves.

(F) GCD curves of the supercapacitor at different strain states from 0% to 300%, measured at the current density of 10 mA cm^{-2} .

(G) Capacitance from the GCD curves at different strain states and current densities.

(H) Capacitance retention of the supercapacitor under 1,000 uniaxially stretching-relaxation cyclic deformations up to 200% strain. Inset shows the CV curves in the relaxed state at 100 mV s^{-1} before and after 1,000 stretching-relaxation cycles.

(I) Capacitance retention of the supercapacitor with 10,000 charge/discharge cycles of 5 mA cm^{-2} at the strain of 0% and 200%. Inset shows the CV curves at 0% strain before and after the electrochemical stability test at the scan rate of 1 V s^{-1} .

Performance of Stretchable Au-CNT Forest Supercapacitors

Figure 6 shows the electrochemical performance of a uniaxially stretchable supercapacitor assembled with two crumpled Au-CNT forest electrodes and poly(vinyl alcohol) (PVA)- H_2SO_4 gel electrolyte (Figure S8). Figure 6A presents the CV curves of the Au-CNT forest supercapacitor in the relaxed state at different scan rates from 50 mV s^{-1} to 5 V s^{-1} . The capacitance of the supercapacitor decreases gradually with the increasing scan rate. However, the shape of the CV curves remains

rectangular even at the high scan rate of 5 V s^{-1} due to the vertically aligned porous structure and the excellent conductivity of the Au-CNT forest. Figures 6B and 6C demonstrate the CV curves of the stretchable supercapacitor at different strain states from 0% to 300%, measured at the scan rates of 100 mV s^{-1} and 5 V s^{-1} , respectively. The CV curves obtained at 100 mV s^{-1} at different strain states are identical, whereas the CV curves at 5 V s^{-1} show slight differences. At the scan rate of 5 V s^{-1} , the current density in the CV of the Au-CNT forest electrode decreases slightly with the applied strain in the whole voltage window (Figure 6C), indicating decreased specific capacitance. This phenomenon is different from the result of a three-electrode experimental setup in which the CV current density increases with the increasing strain. The difference between a single electrode and an all-solid-state device may arise from the different phases of the electrolyte. For a single electrode immersed in electrolyte solution, the electrolyte/electrode interface is the same at different strain states. Therefore, the diffusion resistance dominates the electrochemical behavior of the electrode. However, for an all-solid-state supercapacitor, the interface between the gel electrolyte and the electrodes becomes critical to the electrochemical performance of the device. When the crumpled Au-CNT forest supercapacitor is relaxed from 300% strain to 0% strain, the compression of the device leads to an improved contact between the gel electrolyte and the Au-CNT forest electrodes. The pressure can enhance the specific capacitance of the device significantly due to the reduced diffusion resistance and the reduced interfacial resistance of assembled supercapacitors.^{49–51} As a result, the crumpled Au-CNT forest supercapacitors show enhanced electrochemical performance with the decreased applied strains. It should be mentioned that the CV curve at the strain state of 300% maintains the rectangular shape with considerable capacitance compared with the CV curve in the relaxation state resulting from the Au-CNT bottom network.

Figure 6D presents the Nyquist plot of a crumpled Au-CNT forest supercapacitor at different strain states, revealing that the impedance of an Au-CNT supercapacitor at different strain states is almost constant. Benefiting from the enhanced electric conductivity of the Au-CNT network, the resistance of the device ranges from 3.5Ω to 4.5Ω at different strain states, which is much smaller compared with the crumpled CNT supercapacitors ($100\text{--}260 \Omega$) reported in the literature.²³ The Au-CNT forest supercapacitor is as conductive as most of the thin film supercapacitors yet maintains the discretized feature and accessible porous structure of the CNT forest (Figures 1B–1D). Figure 6E demonstrates the real capacitance of the Au-CNT forest supercapacitor at different strain states for a wide range of frequency from 0.1 Hz to 200 kHz. The device shows similar capacitance (<25% difference) at different strain states in the whole range of frequency. The GCD curves of the device measured at 10 mA cm^{-2} also confirm the analogous capacitance between different strain states (Figure 6F). The charge/discharge time of the device for one cycle at 10 mA cm^{-2} decreases slightly from 1.38 s to 1.22 s when the applied strain increases from 0% to 300%. The specific capacitance of the device is then calculated based on the GCD measurements. The capacitance of the Au-CNT forest supercapacitor is $\sim 12 \text{ mF cm}^{-2}$ at a low current density of 0.5 mA cm^{-2} for all of the applied strains (Figure 6G). When the current density is 40 mA cm^{-2} , the specific capacitance of the device drops to $\sim 6 \text{ mF cm}^{-2}$, corresponding to capacitance retention of $\sim 50\%$. The capacitance retention of the symmetric supercapacitor is lower than that of the single electrode, most likely because of the slower ion mobility in the gel electrolyte. Figures 6H and 6I depict the mechanical and electrochemical stability, respectively, of the stretchable device. The capacitance of the device has negligible reduction after 1,000 stretching-relaxation cycles for up to 200% strain (Figure 6H), exhibiting good mechanical

stability of the Au-CNT electrode and a stable electrode/gel electrolyte interface. It can be seen that the capacitance retention after 10,000 charge/discharge cycles at 10 mA cm^{-2} is $\sim 93.6\%$ for 0% strain and $\sim 94.2\%$ for 200% strain, respectively, indicating the excellent electrochemical stability of the device at different strain states (Figure 6I).

To better evaluate the electrochemical and mechanical performance of the crumpled Au-CNT forest supercapacitor, we compare the specific capacitance and stretchability of crumpled Au-CNT supercapacitor with other CNT-based supercapacitors in the literature, as listed in Table S1.^{52–57} The crumpled Au-CNT forest supercapacitors possess comparable area and volumetric capacitance due to their unique hierarchical structure and high conductivity. In addition, the crumpled Au-CNT supercapacitors exhibit a large mechanical stretchability of 300%, which renders them a promising candidate for high-performance stretchable or wearable energy-storage devices. Furthermore, the crumpled Au-CNT forest supercapacitors demonstrate outstanding rate capability, which is desired for many specific applications requiring a fast charge/discharge rate. Figure S9 further presents the energy density and power density of a crumpled Au-CNT forest supercapacitor and its comparison with other CNT supercapacitors reported in the literature. The crumpled Au-CNT forest supercapacitor has a larger energy and power density compared with our crumpled CNT forest supercapacitors previously reported and the other CNT-based supercapacitors in the literature.

DISCUSSION

In conclusion, a robust and stretchable Au-CNT forest electrode has been developed by sputter coating a thin layer of metal film on top of the CNT forest grown by PECVD. The Au-CNT forest network served as the current collector at the base of stretchable CNT forest electrodes and reduced the electrode resistance by one order of magnitude. Compared with stretchable CNT forest electrodes, the stretchable Au-CNT forest electrodes have demonstrated superior electrochemical performance with improved specific capacitance ($\sim 26 \text{ mF cm}^{-2}$ for biaxially stretchable Au-CNT forest) and excellent rate capability ($\sim 64\%$ from 20 mV s^{-1} to 5 V s^{-1} for uniaxially stretchable Au-CNT forest). Moreover, the stretchable Au-CNT forest electrode maintains its superior electrochemical performance under large mechanical strains (i.e., 800% area strain) in both low and high charge/discharge rates, which cannot be achieved by the reported stretchable CNT forest electrodes. The stretchable Au-CNT forest electrode also exhibited good mechanical stability ($\sim 100\%$ for 1,400 cycles) and electrochemical stability (97.6% for 10,000 cycles). A symmetric stretchable supercapacitor made of uniaxially crumpled Au-CNT forest and PVA- H_2SO_4 gel electrolyte finally demonstrated nearly identical specific capacitance and stable electrochemical performance under different strains. The stretchable Au-CNT forest-based electrodes and supercapacitors are expected to have broad applications in wearable electronics with high power density and fast charge/discharge capability requirements. The crumpled Au-CNT forest can also serve as an electronic scaffold to further enhance its capacitance and energy density by impregnating pseudocapacitive materials.

EXPERIMENTAL PROCEDURES

Fabrication of Crumpled Au-CNT Forest Electrode

The procedures for the growth of CNT forest on silicon wafers are the same as those described in our previous work.²³ The gold film was deposited on top of the CNT forest by using a Desk V Vacuum Sputter System (Denton Vacuum). The deposition

time was 580 s and five depositions were performed consecutively to obtain a ~50-nm-thick Au film. The as-prepared Au-CNT forest was then dry-transferred onto a prestrained elastomer substrate (VHB 4910; 3M, USA). To facilitate the dry transfer of the CNT forest, we annealed the as-grown CNT forest on a Si wafer in air on a hotplate at 540°C for 15 min. The CNT forest was then dry-transferred from the Si wafer onto the prestrained elastomer substrate following the same procedures reported in the literature.²³ The prestrain in the stretched substrate was then relaxed along two orthogonal directions sequentially to form a crumpled Au-CNT forest electrode with hierarchical wrinkle/ridge structures.

Characterization and Measurements of Stretchable Electrode

SEM images of the stretchable CNT and Au-CNT forest were taken with an FEI XL30 microscope and an Apreo S system. ImageJ was used to measure the diameter of CNT and Au-coated CNT. The electrical resistance of the stretchable CNT or Au-CNT forest electrode was measured by using a Flukes 77 IV multimeter. The resistance was measured across the diagonal direction of the stretchable forest. Five measurements were averaged for the reported values.

Electrochemical Measurements of Electrodes

Bio-Logic Sp-200 was used as the potentiostat in all experiments. A three-electrode setup was used to measure the electrochemical performance of the stretchable electrodes. The Ag/AgCl in saturated KCl solution was utilized as the reference electrode. A Pt mesh was used as the counter electrode. All measurements were performed at room temperature in 1 M H₂SO₄ solution. Ti wire was used as the current collector to connect the stretchable electrodes with the potentiostat because of its small capacitance, high conductivity, and low catalytic activity in H₂SO₄. Before each measurement, CV was performed with scan rates from 50 mV s⁻¹ to 100 V s⁻¹ to clean and wet the surfaces. The CV measurements were performed from -0.1 V to 0.8 V with scan rates from 20 mV s⁻¹ to 5 V s⁻¹ for uniaxially stretchable CNT and Au-CNT electrodes. For biaxially stretchable CNT and Au-CNT electrodes, the potential window was chosen to be from 0 V to 0.8 V with the same scan rates. GCD measurements were performed from -0.1 V to 0.8 V with current densities from 0.5 mA cm⁻² to 40 mA cm⁻² for uniaxially stretchable CNT and Au-CNT electrodes. For biaxially stretchable CNT and Au-CNT electrodes, the potential window was chosen to be from 0 V to 0.8 V with current densities from 0.5 mA cm⁻² to 80 mA cm⁻². A smaller potential window was applied for the biaxially stretchable CNT and Au-CNT forest electrodes because below 0 V versus Ag/AgCl, the biaxially stretchable CNT and Au-CNT forest electrodes at large mechanical strains showed higher catalytic currents leading to the misinterpretation of its energy-storage capability. EIS was conducted at 0.4 V versus Ag/AgCl for all stretchable CNT and Au-CNT forest electrodes. The frequency range was from 0.1 Hz to 200 kHz with a potential sinusoidal amplitude of 10 mV. Capacitance was calculated in two ways. The capacitance from CV scans was calculated from both the charge and discharge regions of the CV curves at different scan rates by

$$C = \frac{S}{2v \times (V_a - V_c)},$$

where V_a and V_c are the anodic and cathodic vertex potentials of the CV measurements, v is the scan rate of the CV measurements, and S is the area of the CV curve. The capacitance from GCD is calculated by

$$C = \frac{I \times \Delta t}{V - V_0},$$

where I is the discharge current density of the GCD measurements, Δt is the discharge time, V is the applied potential, and V_o is the ohmic drop at the beginning of the discharge process. The energy density and power density is calculated by

$$E = \frac{1}{2 \times 3,600} C(V - V_o)^2,$$
$$P = \frac{3,600 \times E}{t},$$

where C is the capacitance from the GCD measurement, V_o is the ohmic drop at the beginning of the discharge process, and t is the discharge time. The unit of E and P is respectively Wh m^{-2} and W m^{-2} .

Mechanical stability for a uniaxially stretchable Au-CNT electrode was examined by performing 1,400 uniaxial stretching-relaxation cycles from 0% to 200% strain. The specific capacitance was calculated by using GCD measurements at the current density of 2 mA cm^{-2} . Electrochemical stability was evaluated by testing 10,000 GCD cycles at a current density of 5 mA cm^{-2} . Pt wires were used as current collectors for long-term testing in $1 \text{ M H}_2\text{SO}_4$ electrolyte. The capacitance, energy density, and power density are based on the area of active material in the relaxation state (i.e., 0% and 0% \times 0% strain).

Fabrication and Measurements of Stretchable Supercapacitors

Two and a half grams of PVA (MW 146,000–186,000; Sigma-Aldrich) was dissolved into 25 mL of $1 \text{ M H}_2\text{SO}_4$. The solution was heated up to 90°C for 1 h with stirring until it became clear. The prepared PVA- H_2SO_4 solution was then degassed in a vacuum desiccator overnight to remove the bubbles. The PVA- H_2SO_4 gel was finally cast onto the stretched CNT forest electrodes. A small margin area ($\sim 2 \text{ mm}$) was left uncovered for placing Pt wires for electrochemical measurement. After drying in air for 30 min, the two prestretched CNT forest electrodes were laminated together. The PVA- H_2SO_4 gel (~ 100 – $120 \mu\text{m}$ by vernier calipers) served as both electrolyte and separator in the assembled supercapacitor. The final device was then tested by a standard two-electrode setup. CV curves were measured from 0 V to 0.8 V at the scan rates from 20 mV s^{-1} to 5 V s^{-1} . EIS was performed from 0.1 Hz to 200 kHz with a potential sinusoidal amplitude of 10 mV at 0 V. GCD measurements were done between 0 V and 0.8 V with the current densities varying from 0.5 mA cm^{-2} to 40 mA cm^{-2} . Mechanical stability was evaluated by the discharged capacitance of CV at 100 mV s^{-1} after multiple cyclic mechanical strains. Electrochemical stability was evaluated by performing 10,000 GCD cycles at a current density of 5 mA cm^{-2} . Energy density and power density were calculated in the same way as for the electrode. The capacitance, energy density, and power density are based on the area of active material in the relaxation state.

SUPPLEMENTAL INFORMATION

Supplemental Information can be found online at <https://doi.org/10.1016/j.matt.2020.02.024>.

ACKNOWLEDGMENTS

This work is partially supported by the USDA National Institute of Food and Agriculture (Hatch Project 1016788), NSF (ECCS-1344745), and Startup Fund from Michigan State University. The authors thank Yaying Feng from Duke University for the assistance in preparing samples and images and Maria L. Sartorelli from Duke University for the helpful discussion on EIS measurements. This work was performed in part at the Shared Materials Instrumentation Facility (SMIF) of Duke University, a member of the North Carolina Research Triangle Nanotechnology Network

(RTNN), which is supported by the NSF (ECCS-1542015) as part of the National Nanotechnology Coordinated Infrastructure (NNCI).

AUTHOR CONTRIBUTIONS

Y.Z. and C.C. conceived the concept and designed the experiments. Y.Z. carried out the experiments. Y.C. and Q.H. assisted with experiments and data preparation. All authors analyzed and discussed the data and commented on the manuscript. C.C., Y.Z., and J.T.G. wrote the manuscript.

DECLARATION OF INTERESTS

The authors declare no competing interests.

Received: January 5, 2020

Revised: February 11, 2020

Accepted: February 27, 2020

Published: March 19, 2020

REFERENCES

- Xu, B., Zhu, M., Zhang, W., Zhen, X., Pei, Z., Xue, Q., Zhi, C., and Shi, P. (2016). Ultrathin MXene-micropattern-based field-effect transistor for probing neural activity. *Adv. Mater.* 28, 3333–3339.
- Huang, Y., Hu, H., Huang, Y., Zhu, M., Meng, W., Liu, C., Pei, Z., Hao, C., Wang, Z., and Zhi, C. (2015). From industrially weavable and knittable highly conductive yarns to large wearable energy storage textiles. *ACS Nano* 9, 4766–4775.
- Bao, Z., and Chen, X. (2016). Flexible and stretchable devices. *Adv. Mater.* 28, 4177–4179.
- Lou, Z., Chen, S., Wang, L., Jiang, K., and Shen, G. (2016). An ultra-sensitive and rapid response speed graphene pressure sensors for electronic skin and health monitoring. *Nano Energy* 23, 7–14.
- Cao, C., Chu, Y., Zhou, Y., Zhang, C., and Qu, S. (2018). Recent advances in stretchable supercapacitors enabled by low-dimensional nanomaterials. *Small* 14, e1803976.
- Liu, Y., He, K., Chen, G., Leow, W.R., and Chen, X. (2017). Nature-inspired structural materials for flexible electronic devices. *Chem. Rev.* 117, 12893–12941.
- Wang, Z., Guan, X., Huang, H., Wang, H., Lin, W., and Peng, Z. (2019). Full 3D printing of stretchable piezoresistive sensor with hierarchical porosity and multimodulus architecture. *Adv. Funct. Mater.* 29, 1807569.
- Yao, S., and Zhu, Y. (2015). Nanomaterial-enabled stretchable conductors: strategies, materials and devices. *Adv. Mater.* 27, 1480–1511.
- An, T., Zhu, B., Ling, Y., Gong, S., and Cheng, W. (2019). A janus gold nanowire electrode for stretchable micro-supercapacitors with distinct capacitances. *J. Mater. Chem. A* 7, 14233–14238.
- Mirvakili, S.M., and Hunter, I.W. (2017). Vertically aligned niobium nanowire arrays for fast-charging micro-supercapacitors. *Adv. Mater.* 29, 1700671.
- Meng, Y., Zhao, Y., Hu, C., Cheng, H., Hu, Y., Zhang, Z., Shi, G., and Qu, L. (2013). All-graphene core-sheath microfibers for all-solid-state, stretchable fibriform supercapacitors and wearable electronic textiles. *Adv. Mater.* 25, 2326–2331.
- Wang, H., Wang, C., Jian, M., Wang, Q., Xia, K., Yin, Z., Zhang, M., Liang, X., and Zhang, Y. (2018). Superelastic wire-shaped supercapacitor sustaining 850% tensile strain based on carbon nanotube@graphene fiber. *Nano Res.* 11, 2347–2356.
- Zhao, C., Wang, C., Yue, Z., Shu, K., and Wallace, G.G. (2013). Intrinsically stretchable supercapacitors composed of polypyrrole electrodes and highly stretchable gel electrolyte. *ACS Appl. Mater. Interfaces* 5, 9008–9014.
- Wang, Y., Chen, F., Liu, Z., Tang, Z., Yang, Q., Zhao, Y., Du, S., Chen, Q., and Zhi, C. (2019). A highly elastic and reversibly stretchable all-polymer supercapacitor. *Angew. Chem. Int. Ed.* 58, 15707–15711.
- Zhou, Y., Maleski, K., Anasori, B., Thostenson, J.O., Pang, Y., Feng, Y., Zeng, K., Parker, C.B., Zauscher, S., Gogotsi, Y., et al. (2020). $\text{Ti}_3\text{C}_2\text{T}_x$ MXene-reduced graphene oxide composite electrodes for stretchable supercapacitors. *ACS Nano*. <https://doi.org/10.1021/acsnano.9b10066>.
- Lv, Z., Luo, Y., Tang, Y., Wei, J., Zhu, Z., Zhou, X., Li, W., Zeng, Y., Zhang, W., Zhang, Y., et al. (2018). Editable supercapacitors with customizable stretchability based on mechanically strengthened ultralong MnO_2 nanowire composite. *Adv. Mater.* 30, 1704531.
- Gu, T., and Wei, B. (2016). High-performance all-solid-state asymmetric stretchable supercapacitors based on wrinkled MnO_2/CNT and $\text{Fe}_2\text{O}_3/\text{CNT}$ macrofilms. *J. Mater. Chem. A* 4, 12289–12295.
- Qi, D., Liu, Z., Liu, Y., Leow, W.R., Zhu, B., Yang, H., Yu, J., Wang, W., Wang, H., Yin, S., et al. (2015). Suspended wavy graphene microribbons for highly stretchable microsupercapacitors. *Adv. Mater.* 27, 5559–5566.
- Gao, Z., Zhang, Y., Song, N., and Li, X. (2017). Biomass-derived renewable carbon materials for electrochemical energy storage. *Mater. Res. Lett.* 5, 69–88.
- Yu, C., Masarapu, C., Rong, J., Wei, B., and Jiang, H. (2009). Stretchable supercapacitors based on buckled single-walled carbon-nanotube macrofilms. *Adv. Mater.* 21, 4793–4797.
- Zang, J., Cao, C., Feng, Y., Liu, J., and Zhao, X. (2014). Stretchable and high-performance supercapacitors with crumpled graphene papers. *Sci. Rep.* 4, 6492.
- Dagdeviren, C., Joe, P., Tuzman, O.L., Park, K.-I., Lee, K.J., Shi, Y., Huang, Y., and Rogers, J.A. (2016). Recent progress in flexible and stretchable piezoelectric devices for mechanical energy harvesting, sensing and actuation. *Extreme Mech. Lett.* 9, 269–281.
- Cao, C., Zhou, Y., Ubnoske, S., Zang, J., Cao, Y., Henry, P., Parker, C.B., and Glass, J.T. (2019). Highly stretchable supercapacitors via crumpled vertically aligned carbon nanotube forests. *Adv. Energy Mater.* 9, 1900618.
- Kim, B., Chung, H., and Kim, W. (2012). High-performance supercapacitors based on vertically aligned carbon nanotubes and nonaqueous electrolytes. *Nanotechnology* 23, 155401.
- Amade, R., Jover, E., Caglar, B., Mutlu, T., and Bertran, E. (2011). Optimization of MnO_2 /vertically aligned carbon nanotube composite for supercapacitor application. *J. Power Sources* 196, 5779–5783.
- Hsia, B., Marschewski, J., Wang, S., In, J.B., Carraro, C., Poulidakos, D., Grigoropoulos, C.P., and Maboudian, R. (2014). Highly flexible, all solid-state micro-supercapacitors from

- vertically aligned carbon nanotubes. *Nanotechnology* 25, 055401.
27. Ubnoske, S.M., Raut, A.S., Brown, B., Parker, C.B., Stoner, B.R., and Glass, J.T. (2014). Perspectives on the growth of high edge density carbon nanostructures: transitions from vertically oriented graphene nanosheets to graphenated carbon nanotubes. *J. Mater. Chem. C* 118, 16126–16132.
28. Zhang, R., Ding, J., Liu, C., and Yang, E.-H. (2018). Highly stretchable supercapacitors enabled by interwoven CNTs partially embedded in PDMS. *ACS Appl. Energy Mater.* 1, 2048–2055.
29. Raut, A.S., Parker, C.B., Stoner, B.R., and Glass, J.T. (2012). Effect of porosity variation on the electrochemical behavior of vertically aligned multi-walled carbon nanotubes. *Electrochem. Commun.* 19, 138–141.
30. Brown, B., Parker, C.B., Stoner, B.R., Grill, W.M., and Glass, J.T. (2012). Electrochemical charge storage properties of vertically aligned carbon nanotube films: effects of thermal oxidation. *J. Mater. Chem. C* 116, 19526–19534.
31. Cao, C., Feng, Y., Zang, J., López, G.P., and Zhao, X. (2015). Tunable lotus-leaf and rose-petal effects via graphene paper origami. *Extreme Mech. Lett.* 4, 18–25.
32. Mutha, H.K., Lu, Y., Stein, I.Y., Cho, H.J., Suss, M.E., Laoui, T., Thompson, C.V., Wardle, B.L., and Wang, E.N. (2016). Porosimetry and packing morphology of vertically aligned carbon nanotube arrays via impedance spectroscopy. *Nanotechnology* 28, 05LT01.
33. Lee, J., Stein, I.Y., Devoe, M.E., Lewis, D.J., Lachman, N., Kessler, S.S., Buschhorn, S.T., and Wardle, B.L. (2015). Impact of carbon nanotube length on electron transport in aligned carbon nanotube networks. *Appl. Phys. Lett.* 106, 053110.
34. Maschmann, M.R., Ehlert, G.J., Tawfick, S., Hart, A.J., and Baur, J.W. (2014). Continuum analysis of carbon nanotube array buckling enabled by anisotropic elastic measurements and modeling. *Carbon* 66, 377–386.
35. Wang, C., Zheng, W., Yue, Z., Too, C.O., and Wallace, G.G. (2011). Buckled, stretchable polypyrrole electrodes for battery applications. *Adv. Mater.* 23, 3580–3584.
36. Kong, Q., Bodelot, L., Lebental, B., Lim, Y.D., Shiau, L.L., Gusarov, B., Tan, C.W., Liang, K., Lu, C., Tan, C.S., et al. (2018). Novel three-dimensional carbon nanotube networks as high performance thermal interface materials. *Carbon* 132, 359–369.
37. Hong, S., Lee, J., Do, K., Lee, M., Kim, J.H., Lee, S., and Kim, D.-H. (2017). Stretchable electrode based on laterally combed carbon nanotubes for wearable energy harvesting and storage devices. *Adv. Funct. Mater.* 27, 1704353.
38. Masarapu, C., Zeng, H.F., Hung, K.H., and Wei, B. (2009). Effect of temperature on the capacitance of carbon nanotube supercapacitors. *ACS Nano* 3, 2199–2206.
39. Rangom, Y., Tang, X., and Nazar, L.F. (2015). Carbon nanotube-based supercapacitors with excellent AC line filtering and rate capability via improved interfacial impedance. *ACS Nano* 9, 7248–7255.
40. Lopez, L., Kim, Y., Jierry, L., Hemmerle, J., Boulmedais, F., Schaaf, P., Pronkin, S., and Kotov, N.A. (2018). Electrochemistry on stretchable nanocomposite electrodes: dependence on strain. *ACS Nano* 12, 9223–9232.
41. Burke, A., and Miller, M. (2010). Testing of electrochemical capacitors: capacitance, resistance, energy density, and power capability. *Electrochim. Acta* 55, 7538–7548.
42. Zhang, S., and Pan, N. (2015). Supercapacitors performance evaluation. *Adv. Energy Mater.* 5, 1401401.
43. Yang, K., Cho, K., Yoon, D.S., and Kim, S. (2017). Bendable solid-state supercapacitors with Au nanoparticle-embedded graphene hydrogel films. *Sci. Rep.* 7, 40163.
44. Portet, C., Taberna, P.L., Simon, P., and Flahaut, E. (2005). Influence of carbon nanotubes addition on carbon-carbon supercapacitor performances in organic electrolyte. *J. Power Sources* 139, 371–378.
45. Portet, C., Taberna, P.L., Simon, P., and Laberty-Robert, C. (2004). Modification of Al current collector surface by sol-gel deposit for carbon-carbon supercapacitor applications. *Electrochim. Acta* 49, 905–912.
46. Chmiola, J., Yushin, G., Dash, R., and Gogotsi, Y. (2006). Effect of pore size and surface area of carbide derived carbons on specific capacitance. *J. Power Sources* 158, 765–772.
47. Portet, C., Taberna, P.L., Simon, P., Flahaut, E., and Laberty-Robert, C. (2005). High power density electrodes for carbon supercapacitor applications. *Electrochim. Acta* 50, 4174–4181.
48. Yu, G., Hu, L., Liu, N., Wang, H., Vosgueritchian, M., Yang, Y., Cui, Y., and Bao, Z. (2011). Enhancing the supercapacitor performance of graphene/MnO₂ nanostructured electrodes by conductive wrapping. *Nano Lett.* 11, 4438–4442.
49. Li, K.-B., Shi, D.-W., Cai, Z.-Y., Zhang, G.-L., Huang, Q.-A., Liu, D., and Yang, C.-P. (2015). Studies on the equivalent serial resistance of carbon supercapacitor. *Electrochim. Acta* 174, 596–600.
50. Li, X., Rong, J., and Wei, B. (2010). Electrochemical behavior of single-walled carbon nanotube supercapacitors under compressive stress. *ACS Nano* 4, 6039–6049.
51. Masarapu, C., Wang, L.-P., Li, X., and Wei, B. (2012). Tailoring electrode/electrolyte interfacial properties in flexible supercapacitors by applying pressure. *Adv. Energy Mater.* 2, 546–552.
52. Li, X., Shao, J., Kim, S.-K., Yao, C., Wang, J., Miao, Y.-R., Zheng, Q., Sun, P., Zhang, R., and Braun, P.V. (2018). High energy flexible supercapacitors formed via bottom-up infilling of gel electrolytes into thick porous electrodes. *Nat. Commun.* 9, 2578.
53. Zhang, Z., Wang, L., Li, Y., Wang, Y., Zhang, J., Guan, G., Pan, Z., Zheng, G., and Peng, H. (2017). Nitrogen-doped core-sheath carbon nanotube array for highly stretchable supercapacitor. *Adv. Energy Mater.* 7, 1601814.
54. Li, W.C., Mak, C.L., Kan, C.W., and Hui, C.Y. (2014). Enhancing the capacitive performance of a textile-based CNT supercapacitor. *RSC Adv.* 4, 64890–64900.
55. Lv, T., Yao, Y., Li, N., and Chen, T. (2016). Highly stretchable supercapacitors based on aligned carbon nanotube/molybdenum disulfide composites. *Angew. Chem. Int. Ed.* 55, 9191–9195.
56. Kim, S.-K., Koo, H.-J., Lee, A., and Braun, P.V. (2014). Selective wetting-induced micro-electrode patterning for flexible micro-supercapacitors. *Adv. Mater.* 26, 5108–5112.
57. Liu, L., Ye, D., Yu, Y., Liu, L., and Wu, Y. (2017). Carbon-based flexible micro-supercapacitor fabrication via mask-free ambient micro-plasma-jet etching. *Carbon* 111, 121–127.